# Semi-Dirac Transport and Anisotropic Localization in Polariton Honeycomb Lattices

B. Real[,1,*] O. Jamadi[,1] M. Milićević[,2] N. Pernet[,2] P. St-Jean[,2] T. Ozawa[,3,4] G. Montambaux[,5] I. Sagnes[,2]
A. Lemaître[,2] L. Le Gratiet[,2] A. Harouri[,2] S. Ravets[,2] J. Bloch[,2] and A. Amo[1]

[1]*Univ. Lille, CNRS, UMR 8523—PhLAM—Physique des Lasers Atomes et Molécules, F-59000 Lille, France*
[2]*Université Paris-Saclay, CNRS, Centre de Nanosciences et de Nanotechnologies, 91120, Palaiseau, France*
[3]*Advanced Institute for Materials Research, Tohoku University, Sendai 980-8577, Japan*
[4]*Interdisciplinary Theoretical and Mathematical Sciences Program (iTHEMS), RIKEN, Wako, Saitama 351-0198, Japan*
[5]*Université Paris-Saclay, CNRS, Laboratoire de Physique des Solides, 91405, Orsay, France*

Compression dramatically changes the transport and localization properties of graphene. This is intimately related to the change of symmetry of the Dirac cone when the particle hopping is different along different directions of the lattice. In particular, for a critical compression, a semi-Dirac cone is formed with massless and massive dispersions along perpendicular directions. Here we show direct evidence of the highly anisotropic transport of polaritons in a honeycomb lattice of coupled micropillars implementing a semi-Dirac cone. If we optically induce a vacancylike defect in the lattice, we observe an anisotropically localized polariton distribution in a single sublattice, a consequence of the semi-Dirac dispersion. Our work opens up new horizons for the study of transport and localization in lattices with chiral symmetry and exotic Dirac dispersions.

Graphene presents extraordinary transport properties arising from the particular conical structure of its Dirac cones. At the Dirac energy, electrons behave as chiral relativistic particles with no mass [1]. Remarkable effects arise from this unusual electronic band structure, such as, conical diffraction [2], integer quantum Hall effect at room temperature [3], antilocalization [4] and Klein tunneling [5–8]. While the Dirac cones in graphene are cylindrically symmetric, anisotropic Dirac cones in strained two-dimensional materials have driven much attention due to the possibility of modifying the Fermi surface and implementing directional transport properties. For instance, by tuning the nearest-neighbor and next-nearest-neighbor hoppings between atoms along a given direction in tight-binding models, it has been shown that tilted Dirac cones with asymmetric Dirac velocities in the $x$ and $y$ directions can be engineered [9–18]. They have been predicted to show exotic tunneling properties [19,20] and high temperature superconducting gaps [21].

A peculiar case of Dirac cone manipulation takes place in a honeycomb lattice when two topologically nonequivalent Dirac cones merge in the presence of uniaxial strain [11,14,22,23]. In this case, quasiparticles at the Dirac point behave as massless particles in one spatial direction and as massive ones in the perpendicular direction, in a so-called semi-Dirac cone. The asymmetry of such exotic Dirac cones anticipates highly anisotropic transport and localization properties as studied in a number of theoretical works [11,14,22–26]. However, these properties have been hardly explored experimentally due to the difficulty in

synthesizing two-dimensional materials with the required asymmetric hoppings and low disorder. For instance, semi-Dirac cones have been observed in black phosphorous [27], but no transport studies are available. Artificial systems, such as ultracold atoms [28], lattices of photonic resonators [29,30], and waveguide arrays [31] have shown the possibility of engineering semi-Dirac cones with an exquisite control, and demonstrated the effect of the merging of the Dirac cones on the presence of edge states [30,31]. However, transport and localization properties have not been studied in these artificial systems because of the need to access simultaneously spectral information and particle dynamics.

In this Letter, we experimentally report the highly anisotropic transport and localization properties of polaritons in lattices of semiconductor micropillars [32–34] showing a semi-Dirac dispersion. We reveal the anisotropic transport of polaritons along perpendicular spatial directions with massive and massless dispersions, characteristic of the semi-Dirac cone. Taking advantage of the driven-dissipative nature of polaritons, we induce effective lattice vacancies, which result in localized polariton distributions with an anisotropic decay and confined in a single honeycomb sublattice. Our observations reveal clear evidence of the long-sought anisotropic transport in unconventional Dirac cones, and provide a new route to implement a localized response in lattices with chiral symmetry.

To engineer the semi-Dirac cone Hamiltonian, we employ lattices of semiconductor micropillars. The lattices are fabricated from a planar semiconductor microcavity
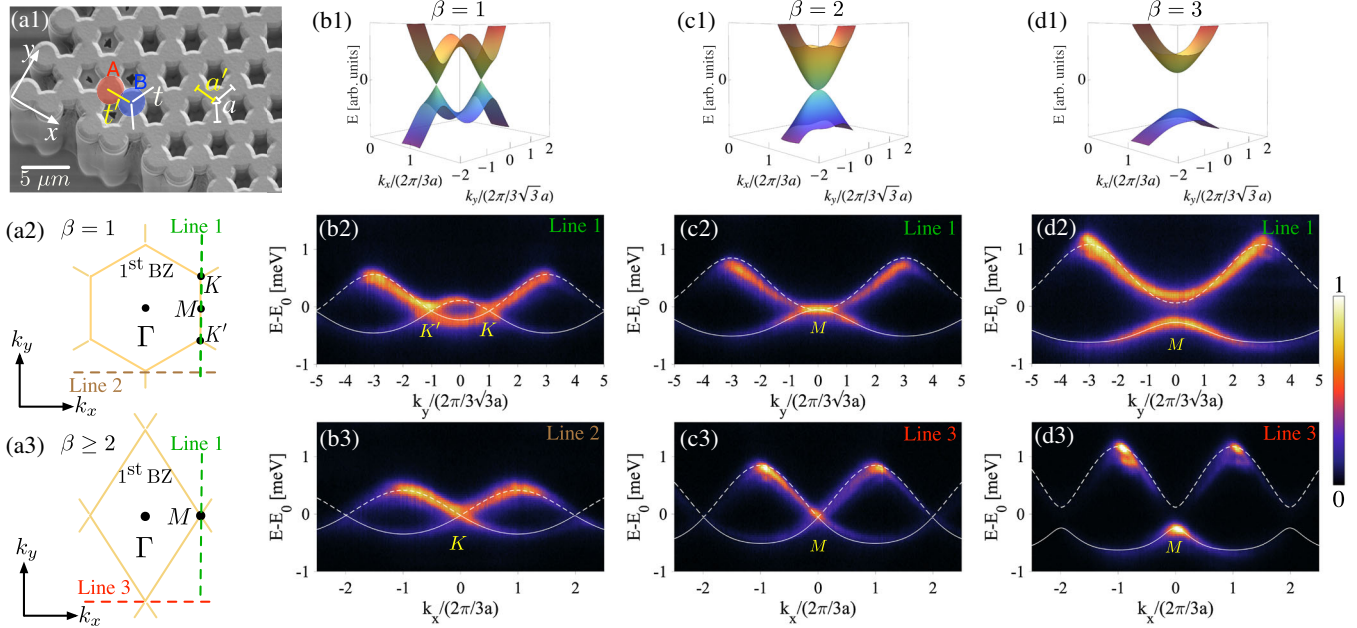
FIG. 1. Dirac cone merging and semi-Dirac dispersion. (a1) Electron microscopy image of a polariton honeycomb lattice. Red and blue circles demarcate $A$ and $B$ sublattices. Yellow and white lines denote hopping among horizontal and diagonal nearest neighbors ($t'$ and $t$, respectively). (a2)–(a3) Sketch of the Brillouin zones in momentum space for $\beta = 1$ and $\beta \geq 2$. Middle and bottom rows of columns (b)–(d) are measured polariton photoluminescence intensity in momentum space for different values of $\beta$. Each image is normalized to its maximum intensity. (b2),(c2),(d2) The emission along $k_y$ for $k_x = 2\pi/3a$ [line 1 in (a2) and (a3)], while (b3),(c3),(d3) exhibit the measurements along $k_x$ for $k_y = -4\pi/3\sqrt{3}a$ (line 2), and for $k_y = -6\pi/3\sqrt{3}a$ (line 3). The white continuous and dashed lines are fits to the lower and upper tight-binding bands [Eq. (1)]. $E_0 = 1589.2$ meV; $a = 2.4$ $\mu$m.

made of 28 (top) and 40 (bottom) pairs of $\lambda/4$ alternating layers of $Ga_{0.05}Al_{0.95}As$ and $Ga_{0.80}Al_{0.20}As$ ($\lambda = 783$ nm), a $\lambda/2$ cavity spacer of $Ga_{0.05}Al_{0.95}As$, and twelve GaAs quantum wells embedded at the three central maxima of the electromagnetic field. At 10 K, the temperature of our experiments, the microcavity is in the strong coupling regime between quantum well excitons and confined photons, giving rise to polaritons characterized by a Rabi splitting of 15 meV. The microcavity is then etched down to the substrate into honeycomb lattices of coupled micropillars of 2.6 $\mu$m diameter. By varying the center-to-center distance between micropillars, the amplitude of the polariton hopping between neighboring micropillars can be engineered [34] to simulate the homogeneous strain that has been predicted to result in semi-Dirac dispersions [11,14,22,23]. All experiments are done at a photon-exciton detuning of −15.2 meV, thus leading to polaritons states with a dominant photonic fraction, which present the longest polariton lifetimes in our samples.

Figure 1(a1) shows a scanning electron microscope image of a lattice with isotropic hoppings, corresponding to a center-to-center distance of $a = a' = 2.4$ $\mu$m for the three nearest-neighbor links of each micropillar. To measure the polariton dispersion and study the transport properties, photoluminescence experiments are done under excitation at the center of the lattice in a spot of 8 $\mu$m with a continuous wave laser at 745 nm. A detailed description of

the experimental setup can be found in the Supplemental Material [35]. Figures 1(b2)–1(b3) show the emission from the lowest energy bands (*s* bands) in momentum space. Along the $k_y$ direction [line 1 in Fig. 1(a2)] two Dirac crossings are observed in Fig. 1(b2), corresponding to the $K$ and $K'$ points characteristic of the unperturbed honeycomb lattice. The Dirac velocities (slopes of the Dirac dispersion) are in this case isotropic around each Dirac cone, as evidenced when comparing the dispersions close to $E_0$ in Fig. 1(b2) for $K$ along $k_y$ [line 1 in Fig. 1(a2)] and in Fig. 1(b3) along $k_x$ [line 2 in Fig. 1(a2)].

The polariton dispersion is well reproduced by a tight-binding model whose eigenvalues are [32,36]

$$E_\pm(\mathbf{k}) = E_0 \pm t\sqrt{(\beta^2 + 2) + f(\mathbf{k})} - \bar{t}f(\mathbf{k}), \quad (1)$$

with, $f(\mathbf{k}) = 2\cos(\sqrt{3}k_y a) + 4\beta\cos([3/2]k_x a) \times \cos([\sqrt{3}/2]k_y a)$, and $E_0$ the Dirac-point energy. $t$ and $\bar{t}$ refer to nearest- (NN) and next-nearest-neighbor (NNN) hoppings, respectively, while $\beta \equiv t'/t$ represents the ratio of the horizontal polariton hopping to the diagonal one [Fig. 1(a1)]. Hence, $\beta$ quantifies the engineered compression strength, which is equal to 1 in the present case (isotropic hopping). A fit of Eq. (1) to the collected photoluminescence [white lines in Figs. 1(b2)–1(b3)] results in the hopping parameters $t = 0.18$ and $\bar{t} = -0.014$ meV. Note that in the

micropillar system, the NNN hopping in Eq. (1) is a phenomenological term that reproduces the observed asymmetry of $s$ bands. Its origin is the coupling of $s$ and $p$ modes, as described in Ref. [37].

When the horizontal hopping $t'$ is increased, the tight-binding bands show that the Dirac cones $K$ and $K'$ move towards each other, and for a value of $\beta = 2$ they merge at a single point [Fig. 1(c1)]. We experimentally probe this situation in Figs. 1(c2)–1(c3) for a lattice with $a' = 2.2$ $\mu$m and $a = 2.4$ $\mu$m. Using the tight-binding model with the previously obtained values of $t$ and $\bar{t}$, a value of $\beta = 2$ reproduces the experimental features. The recorded spectrum along $k_y$ [line 1 in Fig. 1(a3)] shows not only that the two Dirac cones have merged but, more importantly, the dispersions of both the upper and lower bands are now parabolic in this direction, while they remain linear along the $k_x$ direction. This situation is known as a semi-Dirac cone, which combines massless and massive dispersions along perpendicular directions. They have been observed in ARPES measurements of strained black phosphorus [27] and indirectly in various artificial lattices [28–31]. If $\beta$ is further increased, the Dirac cone merging evolves into a band gap [see Fig. 1(d1)]. We implement experimentally this situation by reducing further the center-to-center distance $a'$ to 1.7 $\mu$m as shown in Figs. 1(d2)–1(d3), corresponding to $\beta = 3$.

The anisotropic dispersion of the semi-Dirac cone for $\beta = 2$ is expected to have strong consequences in the transport properties of polaritons. To study this effect, we probe the polariton distribution in real space at different emission energies. Figures 2(a1) and 2(b1) show the real-space intensity at the energy $E_0$ of the Dirac point for $\beta = 1$ and $\beta = 2$, respectively. For $\beta = 1$ [panel (a1)], we observe that polaritons travel away from the excitation spot isotropically; on the contrary for $\beta = 2$ [panel (b1)], the propagation is significantly anisotropic, being more pronounced in the $x$ direction than in the $y$ direction. To quantify this anisotropy, we measure the propagation length on both $x$ and $y$ directions at $E_0$ in both lattices. The propagation length is extracted by fitting an exponential decay to the tails of the emitted intensity, i.e., $|\psi(r)|^2 \propto e^{-r/L_r}$ along the $x$ and $y$ directions [enclosed region in Figs. 2(a1) and 2(b1)]. Experimental points and fits are shown in Figs. 2(a2) and 2(b2). For $\beta = 1$, the propagation lengths are $L_x = 10.21 \pm 2.69$ and $L_y = 9.38 \pm 0.23$ $\mu$m. These values confirm the isotropic transport of polaritons near the Dirac-point energy, which was previously measured in the form of conical diffraction [2]. For $\beta = 2$, at the same energy, we obtain $L_x = 13.31 \pm 1.40$ and $L_y = 4.89 \pm 0.84$ $\mu$m, evidencing the high group velocity in the direction of the massless dispersion, and the reduced group velocity along the $y$ direction associated to the touching parabolic bands.

Figures 2(a3)–2(b4) show in solid dots the measured propagation lengths $L_x$ and $L_y$ as a function of the energy across the Dirac point. This measurement can be directly
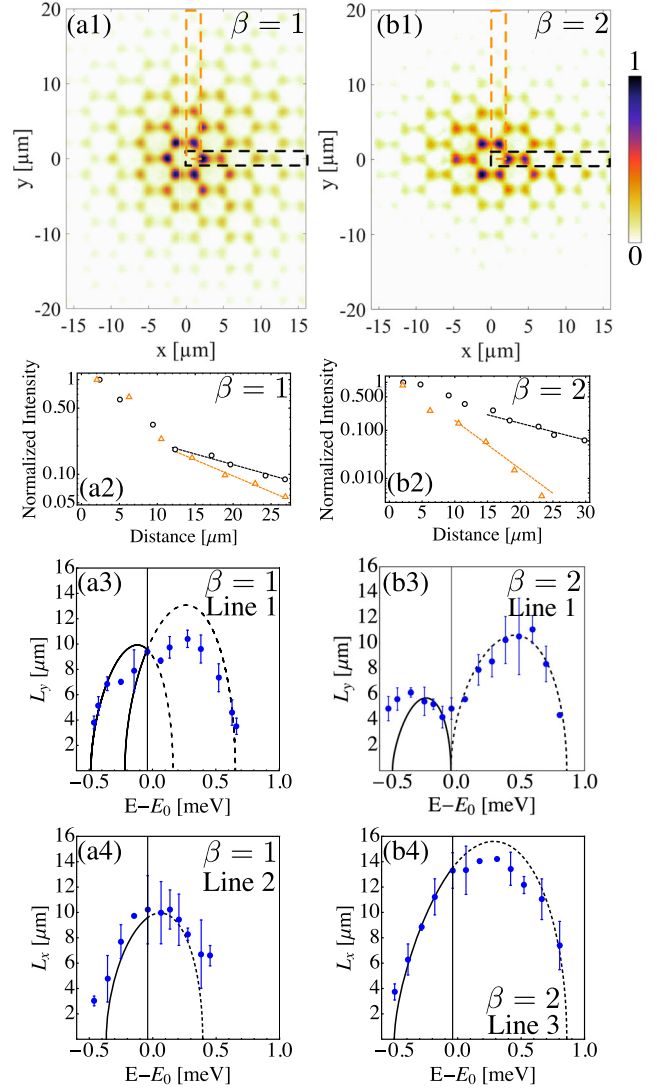


FIG. 2. Transport at the Semi-Dirac point. (a1) and (b1) show the photoluminescence intensity in real space at the energy of the Dirac point ($E_0 = 1589.2$ meV) for $\beta = 1$ and $\beta = 2$, respectively. Each image is normalized to its maximum intensity. (a2)–(b2) The measured intensity along $x$ (circles) and $y$ (triangles) directions for $\beta = 1$ (a2) and $\beta = 2$ (b2), extracted from the dashed boxes in (a1) and (b1). Lines are exponential decay fits. (a3) and (a4) The measured propagation lengths (dots), at several energies, along the $y$ and $x$ directions for $\beta = 1$. (b3) and (b4) Same for $\beta = 2$. Solid and dashed lines display the theoretical propagation lengths [Eq. (2)] corresponding to the solid and dashed bands in Figs. 1(b2), 1(b3), 1(c2), 1(c3). The vertical line depicts the Dirac-point energy $E_0$.

compared to the propagation length expected from the group velocities, $v_{g,x(y)} = \partial E / \partial k_{x(y)}$, in the following way:

$$L_{x(y)} \approx v_{g,x(y)} \tau. \tag{2}$$

$v_{g,x(y)}$ is calculated from the dispersion curves in Fig. 1 along the vertical ($k_x = 2\pi/3a$) and horizontal ($k_y = -4\pi/3\sqrt{3}a$ for $\beta = 1$; $k_y = -6\pi/3\sqrt{3}a$ for $\beta = 2$) directions, and $\tau$ is

the polariton lifetime. The lines in Figs. 2(a3)–2(b4) show the propagation lengths calculated from the group velocities predicted by the tight-binding model in each spatial direction below (continuous line) and above (dashed line) $E_0$. Here we assume a polariton lifetime of $\tau = 14$ and $\tau = 12$ ps, for $\beta = 1$ and $\beta = 2$ lattices, respectively, which is used as a fitting parameter to the experimental points.

The calculated propagation distances match well the experimental data and reproduce the increase of the propagation length along the $x$ direction when going from $\beta = 1$ to $\beta = 2$, due to the higher hopping in that direction [see Figs. 2(a4)–2(b4)]. Along the $y$ direction, the expected propagation length for $\beta = 2$ goes down to zero at the Dirac-point energy $E_0$, a consequence of the massive dispersion along that direction [see Fig. 2(a3)]. Similarly, the calculated propagation length is also zero at the top and bottom of the bands. Experimentally, the measured propagation length at those points is about 4 $\mu$m. This value is, in part, determined by the linewidth of 0.060 meV associated to the finite polariton lifetime: when selecting a given energy, we are in fact detecting the emission from a small range of energies around the desired one, corresponding to states with a nonzero group velocity. Moreover, diffusion of photoexcited excitons away from the excitation spot might also contribute to the residual measured propagation distance.

Further insights on the transport properties at the semi-Dirac cone energy $E_0$ can be accessed when implementing a resonant-laser excitation scheme. Figure 3(a) shows the measured intensity when a resonant laser at $E_0$ is focused on a single micropillar of the $A$ sublattice (marked with a circle) in a lattice with $\beta = 2$. To measure the propagation away from the excitation spot, a mask was placed at the center of the image (white area) with the aim of blocking the excitation beam reflecting onto the CCD (the inset shows an image of the reflected pump beam in the absence of the mask). The image shows some stray laser light close to the excitation spot and a decay of the luminescence on the $B$ sublattice towards the right of the excitation spot. If the excitation is centered on a pillar of the $B$ sublattice, the decay direction and the sublattice asymmetry are reversed, as shown in Fig. 3(c). Further data analysis can be found in Ref. [35].

This behavior is well reproduced using a driven-dissipative model of the polariton dynamics in resonant excitation [38]:

$$i\hbar \frac{\partial \psi_n}{\partial t} = \sum_{m \neq n} t_{n,m} \psi_m - i\frac{\hbar}{\tau} \psi_n + F\delta_{n,n_p} e^{i\omega_p t}. \quad (3)$$

$\psi_n$ represents the polariton amplitude at site $n$, $t_{n,m}$ is the nearest-neighbor hopping, and $F$ is the strength of the pump at frequency $\omega_p$. Figure 3(b) depicts the steady-state solution in the conditions of Fig. 3(a): $\tau = 12$ ps, $t = 0.18$ meV, $\beta = 2$. It shows that the population in the
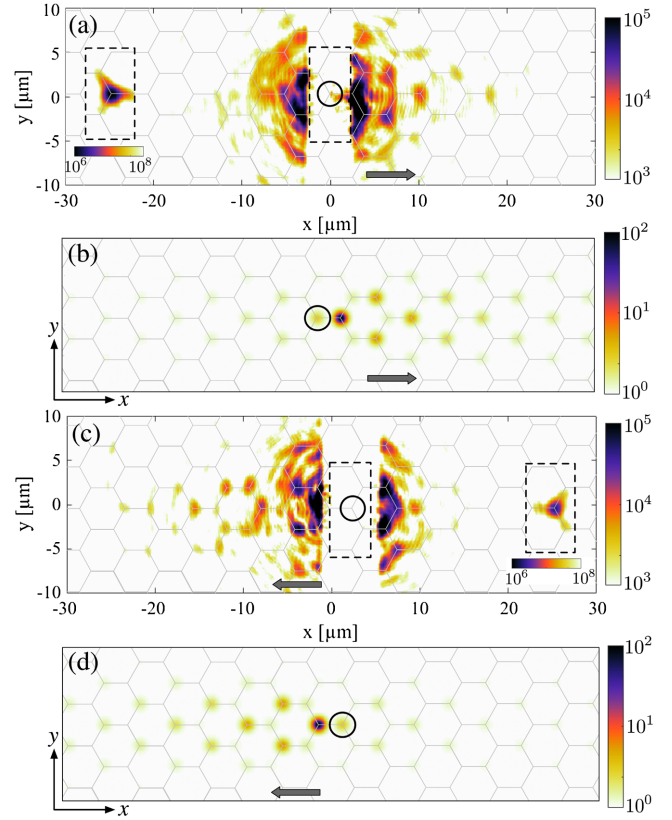


FIG. 3. All-optical analog of a vacancy localization in semi-Dirac graphene. (a) and (b) The measured photoluminescence intensity in real space at the energy of the Dirac point when a single pillar is pumped (demarcated by a circle) in an $A$ pillar (a) and in a $B$ pillar (c). Insets show the reflected pump spot when the beam block is removed from the central region. (b) and (d) The polariton distribution calculated from Eq. (3) when a single $A$ and $B$ pillar, respectively, is pumped at $E_0$ energy. Hexagons depict the underlying lattice.

pumped micropillar, marked by a circle, is almost zero, and the distribution extends mainly to the right of the excited micropillar, on the $B$ sublattice. When moving the excitation spot to a $B$ site [Fig. 3(d)], the distribution reverses its decay direction, as observed in the experiment [panel (c)]. Note that along the $y$ direction, corresponding to the massive dispersion of the semi-Dirac point, the polariton distribution is localized within a single hexagon.

The observed polariton distributions resemble the predicted wave function of electrons bound to a single bulk vacancy in compressed graphene [24]. It has been shown that a single bulk vacancy in graphene creates a defect state at the Dirac-point energy $E_0$, with a decay in amplitude following a $1/r$ law [24,39,40]. The chiral symmetry of the lattice imposes that its wave function resides in one sublattice only: the sublattice opposite to that of the vacancy. Experiments shown in Ref. [35] for lattices with $\beta = 1$ reproduce this situation. In the case of a semi-Dirac cone, the wave function of the vacancy state acquires an

anisotropic distribution: if the vacancy is in the $A$ sublattice, the state is localized to the right of the vacancy; if the vacancy is in the $B$ sublattice, it is localized to the left [24]. In both cases the decay of the amplitude follows $1/\sqrt{|x|}$. These vacancy states are expected to play an important role in the transport properties of graphenelike materials in which localization by weak disorder is strongly decreased due to the Klein tunneling effect.

The similarity between the measured polaritonic distribution and bound electron wave functions can be interpreted phenomenologically as follows. Under resonant excitation ($\hbar\omega_p = E_0$), the population of the driven micropillar interferes destructively with the laser, resulting in an almost zero population in the pumped micropillar, analogous to the effect of a vacancy. This phenomenon was recently reported in the case of two coupled micropillars [41], and it is expected to happen in any lattice of micropillars with chiral symmetry.

In summary, we have probed the simultaneous massive and massless behavior of polaritons in a semi-Dirac honeycomb lattice. Additionally, we have generated an all-optical analog of a vacancy and reported the associated anisotropic distribution in the bulk of the lattice. The use of polariton nonlinearities, absent in the experiments presented here, are a promising perspective for the study of nonlinear modes at Dirac and semi-Dirac points [42], hardly studied so far due to the rarity of systems with engineered Dirac cones and nonlinearities.

---

[*]Corresponding author.
bastian.realelgueda@univ-lille.fr

[1] K. S. Novoselov, A. K. Geim, S. V. Morozov, D. Jiang, M. I. Katsnelson, I. V. Grigorieva, S. V. Dubonos, and A. A. Firsov, Two-dimensional gas of massless Dirac fermions in graphene, Nature (London) **438**, 197 (2005).

[2] O. Peleg, G. Bartal, B. Freedman, O. Manela, M. Segev, and D. N. Christodoulides, Conical Diffraction and Gap Solitons in Honeycomb Photonic Lattices, Phys. Rev. Lett. **98**, 103901 (2007).

[3] K. S. Novoselov, Z. Jiang, Y. Zhang, S. V. Morozov, H. L. Stormer, U. Zeitler, J. C. Maan, G. S. Boebinger, P. Kim, and A. K. Geim, Room-temperature quantum Hall effect in graphene, Science **315**, 1379 (2007).

[4] X. Wu, X. Li, Z. Song, C. Berger, and W. A. de Heer, Weak Antilocalization in Epitaxial Graphene: Evidence for Chiral Electrons, Phys. Rev. Lett. **98**, 136801 (2007).

[5] N. Stander, B. Huard, and D. Goldhaber-Gordon, Evidence for Klein Tunneling in Graphene $p$-$n$ Junctions, Phys. Rev. Lett. **102**, 026807 (2009).

[6] A. F. Young and P. Kim, Quantum interference and Klein tunnelling in graphene heterojunctions, Nat. Phys. **5**, 222 (2009).

[7] P. E. Allain and J. N. Fuchs, Klein tunneling in graphene: Optics with massless electrons, Eur. Phys. J. B **83**, 301 (2011).

[8] T. Ozawa, A. Amo, J. Bloch, and I. Carusotto, Klein tunneling in driven-dissipative photonic graphene, Phys. Rev. A **96**, 013813 (2017).

[9] C. H. Park, L. Yang, Y. W. Son, M. L. Cohen, and S. G. Louie, Anisotropic behaviours of massless Dirac fermions in graphene under periodic potentials, Nat. Phys. **4**, 213 (2008).

[10] M. O. Goerbig, J. N. Fuchs, G. Montambaux, and F. Piéchon, Tilted anisotropic Dirac cones in quinoid-type graphene and $\alpha$-(BEDT-TTF)$_2$I$_3$, Phys. Rev. B **78**, 045415 (2008).

[11] B. Wunsch, F. Guinea, and F. Sols, Dirac-point engineering and topological phase transitions in honeycomb optical lattices, New J. Phys. **10**, 103027 (2008).

[12] P. Dietl, F. Piéchon, and G. Montambaux, New Magnetic Field Dependence of Landau Levels in a Graphenelike Structure, Phys. Rev. Lett. **100**, 236405 (2008).

[13] V. M. Pereira, A. H. Castro Neto, and N. M. R. Peres, Tight-binding approach to uniaxial strain in graphene, Phys. Rev. B **80**, 045401 (2009).

[14] G. Montambaux, F. Piéchon, J.-N. Fuchs, and M. O. Goerbig, Merging of Dirac points in a two-dimensional crystal, Phys. Rev. B **80**, 153412 (2009).

[15] G. Montambaux, F. Piéchon, J.-N. Fuchs, and M. O. Goerbig, A universal Hamiltonian for motion and merging of Dirac points in a two-dimensional crystal, Eur. Phys. J. B **72**, 509 (2009).

[16] R. de Gail, J.-N. Fuchs, M. Goerbig, F. Piéchon, and G. Montambaux, Manipulation of Dirac points in graphene-like crystals, Physica (Amsterdam) **407B**, 1948 (2012).

[17] J. Ibañez-Azpiroz, A. Eiguren, A. Bergara, G. Pettini, and M. Modugno, Self-consistent tight-binding description of Dirac points moving and merging in two-dimensional optical lattices, Phys. Rev. A **88**, 033631 (2013).

[18] J. Feilhauer, W. Apel, and L. Schweitzer, Merging of the Dirac points in electronic artificial graphene, Phys. Rev. B **92**, 245424 (2015).

[19] G. E. Volovik and K. Zhang, Black hole and hawking radiation by type-II Weyl fermions, JETP Lett. **104**, 645 (2016).

[20] V. H. Nguyen and J.-C. Charlier, Klein tunneling and electron optics in Dirac-Weyl fermion systems with tilted energy dispersion, Phys. Rev. B **97**, 235113 (2018).

[21] D. Li, B. Rosenstein, B. Y. Shapiro, and I. Shapiro, Effect of the type-I to type-II Weyl semimetal topological transition on superconductivity, Phys. Rev. B **95**, 094513 (2017).

[22] Y. Hasegawa, R. Konno, H. Nakano, and M. Kohmoto, Zero modes of tight-binding electrons on the honeycomb lattice, Phys. Rev. B **74**, 033413 (2006).

[23] S.-L. Zhu, B. Wang, and L.-M. Duan, Simulation and Detection of Dirac Fermions with Cold Atoms in an Optical Lattice, Phys. Rev. Lett. **98**, 260402 (2007).

[24] C. Dutreix, L. Bilteanu, A. Jagannathan, and C. Bena, Friedel oscillations at the Dirac cone merging point in anisotropic graphene and graphenelike materials, Phys. Rev. B **87**, 245413 (2013).

[25] L.-K. Lim, J.-N. Fuchs, and G. Montambaux, Bloch-Zener Oscillations across a Merging Transition of Dirac Points, Phys. Rev. Lett. **108**, 175303 (2012).

[26] P. Adroguer, D. Carpentier, G. Montambaux, and E. Orignac, Diffusion of Dirac fermions across a topological merging transition in two dimensions, Phys. Rev. B **93**, 125113 (2016).

[27] J. Kim, S. S. Baik, S. H. Ryu, Y. Sohn, S. Park, B.-G. Park, J. Denlinger, Y. Yi, H. J. Choi, and K. S. Kim, Observation of tunable band gap and anisotropic Dirac semimetal state in black phosphorus, Science **349**, 723 (2015).

[28] L. Tarruell, D. Greif, T. Uehlinger, G. Jotzu, and T. Esslinger, Creating, moving and merging Dirac points with a Fermi gas in a tunable honeycomb lattice, Nature (London) **483**, 302 (2012).

[29] M. Bellec, U. Kuhl, G. Montambaux, and F. Mortessagne, Topological Transition of Dirac Points in a Microwave Experiment, Phys. Rev. Lett. **110**, 033902 (2013).

[30] M. Bellec, U. Kuhl, G. Montambaux, and F. Mortessagne, Manipulation of edge states in microwave artificial graphene, New J. Phys. **16**, 113023 (2014).

[31] M. C. Rechtsman, Y. Plotnik, J. M. Zeuner, D. Song, Z. Chen, A. Szameit, and M. Segev, Topological Creation and Destruction of Edge States in Photonic Graphene, Phys. Rev. Lett. **111**, 103901 (2013).

[32] T. Jacqmin, I. Carusotto, I. Sagnes, M. Abbarchi, D. D. Solnyshkov, G. Malpuech, E. Galopin, A. Lemaître, J. Bloch, and A. Amo, Direct Observation of Dirac Cones and a Flatband in a Honeycomb Lattice for Polaritons, Phys. Rev. Lett. **112**, 116402 (2014).

[33] S. Klembt, T. H. Harder, O. A. Egorov, K. Winkler, R. Ge, M. A. Bandres, M. Emmerling, L. Worschech, T. C. H. Liew, M. Segev, C. Schneider, and S. Höfling, Exciton-polariton topological insulator, Nature (London) **562**, 552 (2018).

[34] M. Milićević, G. Montambaux, T. Ozawa, O. Jamadi, B. Real, I. Sagnes, A. Lemaître, L. Le Gratiet, A. Harouri, J. Bloch, and A. Amo, Type-III and Tilted Dirac Cones Emerging from Flat Bands in Photonic Orbital Graphene, Phys. Rev. X **9**, 031010 (2019).

[35] See Supplemental Material at http://link.aps.org/supplemental/10.1103/PhysRevLett.125.186601 for description of the experimental setup, additional experimental data and data analysis.

[36] A. H. Castro Neto, F. Guinea, N. M. R. Peres, K. S. Novoselov, and A. K. Geim, The electronic properties of graphene, Rev. Mod. Phys. **81**, 109 (2009).

[37] F. Mangussi, M. Milićević, I. Sagnes, L. L. Gratiet, A. Harouri, A. Lemaître, J. Bloch, A. Amo, and G. Usaj, Multi-orbital tight binding model for cavity-polariton lattices, J. Phys. Condens. Matter **32**, 315402 (2020).

[38] I. Carusotto and C. Ciuti, Quantum fluids of light, Rev. Mod. Phys. **85**, 299 (2013).

[39] V. M. Pereira, F. Guinea, J. M. B. Lopes dos Santos, N. M. R. Peres, and A. H. C. Neto, Disorder Induced Localized States in Graphene, Phys. Rev. Lett. **96**, 036801 (2006).

[40] T. O. Wehling, A. V. Balatsky, M. I. Katsnelson, A. I. Lichtenstein, K. Scharnberg, and R. Wiesendanger, Local electronic signatures of impurity states in graphene, Phys. Rev. B **75**, 125425 (2007).

[41] S. R. K. Rodriguez, A. Amo, I. Sagnes, L. Le Gratiet, E. Galopin, A. Lemaître, and J. Bloch, Interaction-induced hopping phase in driven-dissipative coupled photonic microcavities, Nat. Commun. **7**, 11887 (2016).

[42] Z. Chen and B. Wu, Bose-Einstein Condensate in a Honeycomb Optical Lattice: Fingerprint of Superfluidity at the Dirac Point, Phys. Rev. Lett. **107**, 065301 (2011).